8422 *Biochemistry* **2009,** *48,* 8422–8434
DOI: 10.1021/bi900606y

BIOCHEMISTRY
including biophysical chemistry & molecular biology
Article

Transmembrane Topology of the Mammalian Slc11a2 Iron Transporter[†]

Maciej Czachorowski,[‡] Steven Lam-Yuk-Tseung,[‡] Mathieu Cellier,[§] and Philippe Gros*[,‡]

[‡]*Department of Biochemistry, McGill University, Montreal, Quebec, Canada H3G-0B1, and* [§]*Institut National de la Recherche Scientifique, INRS-Institut Armand-Frappier, Laval, Quebec, Canada*

Received April 8, 2009; Revised Manuscript Received July 17, 2009

ABSTRACT: The mammalian Slc11a1 and Slc11a2 proteins define a large family of secondary metal transporters. Slc11a1 and Slc11a2 function as pH-dependent divalent cation transporters that play a critical role in host defenses against infections and in Fe^{2+} homeostasis, respectively. The position and polarity of individual transmembrane domains (TMD) of Slc11a2 were studied by an epitope tagging method based on the insertion of small antigenic hemagglutinin A (HA) peptides (YPYDVPDYAS) in predicted intra- or extracellular loops of the protein. The tagged proteins were expressed in transfected LLC-PK1 kidney cells and tested for transport activity, and the polarity of inserted tags with respect to the plasma membrane was determined by immunofluorescence in intact and permeabilized cells. HA epitope tags were inserted at positions 1, 98, 131, 175, 201, 243, 284, 344, 403, 432, 468, 504, and 561. Insertions at positions 98, 131, 175, 403, and 432 abrogated metal transport by Slc11a2, while insertions at positions 1, 201, 243, 284, 344, 468, 504, and 561 resulted in functional proteins. Topology mapping in functional HA-tagged Slc11a2 proteins indicated that the N-terminus (1), as well as loops delineated by TMD4−5 (201), TMD6−7 (284), and TMD10−11 (468), and C-terminus (561) are intracellular, while loops separating TMD5−6 (243), TMD7−8 (344), and TMD11−12 (504) are extracellular. These results are compatible with a topology of 12 transmembrane domains, with intracellular amino and carboxy termini. Structural models constructed by homology threading support this 12TMD topology and show 2-fold structural symmetry in the arrangement of membrane helices for TM1−5 and TM6−10 (conserved Slc11 hydrophobic core).

The Slc11 family of divalent cation transporters has two members in mammals, Slc11a1 (also known as Nramp1)[1] and Slc11a2 (Nramp2, DMT1), which are integral membrane phosphoglycoproteins of 90−100 kDa sharing 64% amino acid sequence identity and 78% similarity (*1*, *2*). Slc11a1 is expressed in the lysosomal compartment of macrophages and in tertiary granules of neutrophils and is rapidly recruited to the membrane of microbe-containing phagosomes formed in these cells (*3*, *4*). At that site, Slc11a1 functions as a pH-dependent efflux pump for Fe^{2+} and Mn^{2+}, restricting the availability of these essential metals to the enclosed microorganisms and contributing to the antimicrobial defenses of macrophages (*5*−*7*). In mice, naturally occurring (G169D) or experimentally induced mutations in *Slc11a1* cause susceptibility to a number of infections including *Mycobacterium*, *Salmonella*, and *Leishmania* (*2*). Likewise, polymorphic variants within or in proximity of the human *SLC11A1* gene have been found to be associated with increased susceptibility to tuberculosis and leprosy in several populations from areas of endemic disease (*8*, *9*). The Slc11a2 protein is expressed at the brush border of the duodenum where it mediates acquisition of non-heme dietary iron. It is also expressed in the syntaxin-13 positive recycling endosome compartment of many cell types, where it is responsible for the transport of transferrin iron from the lumen of acidified endosomes into the cytoplasm (*10*−*12*). Differential splicing of 3′-exons of the *Slc11a2* gene yields two mRNAs with different 3′-end sequences distinguished by the presence (isoform I) or absence (isoform II) of an iron response element (IRE). The two isoforms encoded by these mRNAs also have distinct C-terminal amino acid sequences (*1*). Although both isoforms I and II are present at the plasma membrane, they are expressed in generally different cell types and have distinct organellar distributions and intracellular trafficking properties. Isoform II is present in recycling endosomes while isoform I is present in late endosomes (*13*). Slc11a2 proteins play a central role in iron homeostasis, and a loss-of-function mutation (G185R) causes very severe microcytic anemia in the *mk* mouse and in the *Belgrade* rat (*14*, *15*). In addition, a number of loss-of-function missense (R416C, G212V, delV114) (*16*−*18*) and splicing mutations (*18*, *19*) have been detected in the human *SLC11A2* gene in patients suffering from hypochromic microcytic anemia with serum and liver iron overload.

In transfected mammalian cells, transport studies using isotopic $^{55}Fe^{2+}$ and $^{54}Mn^{2+}$ or the metal-sensitive fluorescent dyes (e.g., calcein and FURA-2) have established that Slc11a1 and Slc11a2 can transport both metals in a pH-dependent fashion (*20*). Experiments in *Xenopus* oocytes have shown that Slc11a2 is a high-affinity transporter for a number of divalent cations (in addition to Fe^{2+} and Mn^{2+}). Transport is electrogenic and is caused by proton movement through the transporter (substrate-dependent and substrate-independent H^+ leak) (*21*, *22*). Sequence analyses show that Slc11 forms a family of metal transporters highly conserved from bacteria to humans. Functional studies on the yeast (*Smf1*−*3*), insect (*Malvolio*), and plant

[†]This work was supported by grants to P.G. from the NIH (NIAID, RO1AI035237). P.G. is a James McGill Professor of Biochemistry.

*To whom correspondence should be addressed. Phone: 514-398-7291. Fax: 514-398-2603. E-mail: philippe.gros@mcgill.ca.

[1]Abbreviations: TMD, transmembrane domains; HA, hemagglutinin A; OPD, *o*-phenylenediamine dihydrochloride; DMT1, divalent metal transporter-1; Nramp, natural resistance-associated macrophage protein; CTM, conserved transport motif.

 Published on Web 07/21/2009

(*AtNramp1−6*) relatives, including yeast complementation experiments in *Smf1−3* knockout strains, indicate that Slc11 proteins share similar function, substrate, and mechanism of transport (*1*, *2*). Strikingly, even these distantly related Slc11 proteins show a number of highly conserved structural features which, through functional characterization experiments, have been shown to play key roles in the mechanism of transport. These structural features include (a) a number of predicted membrane spanning domains (TMD), some of which have amphipathic properties (*23*), (b) several highly conserved charged amino acid residues within these predicted TMDs, with mutations at several negatively charged positions (D86, E154, D192, E299) abrogating transport (*24*), (c) a pair of invariant histidines (H267, H272) in predicted TMD6 that play a key role in pH regulation of transport and/or H^+ movement through the transporter (*23*, *24*), (d) a mutation-sensitive segment at the C-terminal end of predicted TMD1 (*25−27*), (e) a highly conserved sequence motif (residues 384−403), in which alterations abrogate transport (*28*), and (f) a cluster of predicted Asn-linked glycosylation sites in an otherwise poorly conserved segment delineated by predicted TMD7 and 8. Finally, a functional fish Slc11γ transporter lacking predicted TMD11 and 12 has been described, suggesting that the first ten TMDs constitute the main functional unit of this family of transporters (*29*).

High-resolution structural information is ultimately required not only to understand the mechanism of metal transport by Slc11 proteins but also to determine how conserved, mutation-sensitive regions of the transporters coordinate simultaneous metal and H^+ transport. Determining the secondary structure of Slc11 proteins is a necessary first step toward this goal. A combination of multiple sequence alignments, hydropathy profiling, hydrophobic moments, and other predictive methods has been used to propose that Slc11 proteins from animals contain 12 TMD, while yeast and microbial proteins would contain 11 (*23*). Immunofluorescence studies have shown that the amino and carboxyl termini of mouse Slc11a2 are intracellular (*30*, *31*) while the glycosylated loop between predicted TMDs 7 and 8 is extracytoplasmic in Slc11a1 and Slc11a2 (*20*). These studies suggest a model in which the N- and C-termini are intracellular with an even number of 12 TM domains. Although parallel topology studies of the *Escherichia coli* transporter (MntH) support this model (*32*), one study using an anti-Slc11a1 antibody to inhibit Fe^{2+} transport suggests that the N- and C-termini of Slc11a1 are extracytoplasmic (*33*).

In the present study, we investigated the topology of the mammalian Slc11a2 protein, including the number, position, and orientation of individual transmembrane domains. For this, we used a hemagglutinin A (HA) epitope-tagging approach in which the membrane topology of the inserted exofacial epitopes is established in transport-competent proteins expressed at the plasma membrane of LLC-PK1 kidney cells. The transmembrane topology obtained experimentally was used to test three-dimensional models of the 10 TMD structural fold that is conserved among several families of cation-driven transporters.

EXPERIMENTAL PROCEDURES

Materials. Reagent grade chemicals were purchased from Sigma Chemicals (St. Louis, MO). Geneticin (G418) was obtained from Invitrogen. Monoclonal mouse antibody (HA.11) directed against the influenza hemagglutin epitope (HA) was purchased from Covance (Berkeley, CA). Calcein acetoxymethyl ester (calcein-AM) was purchased from Molecular Probes (Eugene, OR). Cy3-conjugated goat anti-mouse secondary antibodies and peroxidase-coupled donkey anti-mouse and goat anti-rabbit antisera were purchased from Jackson ImmunoResearch Laboratories (West Grove, PA). All restriction enzymes and Vent DNA polymerase were obtained from New England Biolabs (Ipswich, MA).

Plasmids and Site-Directed Mutagenesis. The construction of the full-length cDNA for murine *Slc11a2* isoform II (−IRE) cloned into the *Hin*dIII site of pCB6 (pN2-2myc) was described elsewhere (*24*). The construction of *Slc11a2* isoform I (+IRE) full-length cDNA in pCB6 and containing a hemagglutinin (HA) tag in the fourth predicted extracellular loop (pN2-HAIRE) has been described (*13*). The *Slc11a2* isoform II cDNA was excised from pN2-2myc by *Hin*dIII digestion and cloned into pBluescript KS+ (Stratagene, LaJolla, CA) modified by the elimination of the *Sac*I and *Xba*I sites from the polylinker to generate pN2myc-B/S-KO. To improve protein expression in transfected cells, the full-length *Slc11a2* cDNA was modified at its 5′-end by the addition of a consensus GCCACC Kozak sequence and additional *Eco*RI, *Mlu*I, and *Hin*dIII sites to enable subsequent cloning into the mammalian expression vector pCB6 (*31*). This was done by PCR mutagenesis, using oligonucleotide primers EMHK-NT F (5′-CAGAATTCACGCGTAAGCTT***GCCACC***ATGGTGTTGGATCCTAAAGAAAAGATG-3′) and N2 501 R (5′-GCCAATGACTTCCTGCATGTC-3′) and pN2-HAIRE as a template. The 3′-end of *Slc11a2* in pN2myc-B/S-KO was modified to replace isoform II-specific 3′-end sequences with isoform I sequences, using PCR mutagenesis with oligonucleotides N2 1051 F (5′-ACTCTGGCTGTGGACATCTAC-3′) and N2-I-CT-HX R (5′-CAGTCTCGAGAAGCTTTTACTTAATGTTGCCACCGCTGG-3′) with pN2-HAIRE as the template. These modified 5′ (N-terminal) and 3′ (C-terminal) fragments of *Slc11a2* were then subcloned as *Eco*RI/*Bst*EII and *Sac*I/*Xho*I fragments, respectively, into pN2myc-B/S-KO to generate the final construct pN2IRE-B/S-KO.

HA epitopes (YPYDVPDYAS) were inserted in the mouse Slc11a2 (+IRE) protein (*13*) by recombinant PCR (*34*) and using mutagenic primers listed in Table 1. To facilitate the potential insertion of additional HA epitopes, a *Nhe*I restriction site was inserted at the 3′-end of each HA sequence, accounting for the additional S residue found at the C-terminus of each HA tag. pN2-HAIRE was used as a template for all mutagenesis reactions, except for construct 6 for which pN2-2myc was used as a template. The modified *Slc11a2* products were then digested and subcloned as either *Eco*RI/*Bst*EII (constructs NT and 1), *Bst*EII/*Xba*I (constructs 2, 3, 4, and 5), *Xba*I/*Sac*I (construct 6), or *Sac*I/*Xho*I (constructs 8, 9, 10, 11, and CT) fragments into pN2IRE-B/S-KO. All constructs were sequenced to verify the absence of undesired mutations, prior to subcloning of each HA-tagged full-length *Slc11a2* fragment into the *Hin*dIII site of pCB6 for transfection. In the case of constructs 5b, 8b, and 11b, a second HA epitope was inserted by cloning a short double-stranded fragment composed of two complementary oligonucleotides into the engineered *Nhe*I sites of the previously inserted HA epitope sequences.

Cell Culture, Transfection, and Western Blotting. LLC-PK1 cells (*35*) were grown in Dulbecco's modified Eagle's medium (Invitrogen) supplemented with 10% fetal bovine serum and 100 units/mL penicillin/streptomycin (37 °C, 5% CO_2). Cells were transfected with different *Slc11a*-HA/pCB6 constructs

Table 1: Oligonucleotides Used for Epitope Insertion by Site-Directed Mutagenesis

		M1[b]		V2	
NT		CA GAA TTC ACG CGT AAG CTT GCC ACC ATG	(HA)[c]	GTG TTG GAT CCT AAA GAA AAG ATG	(27)
		A98		V99	
1	(271)[a]	GAA TCT GAT TTG CAG TCT GGA GCA	(HA)	GTG GCT GGA TTT AAG CTG CTC TG	(317)
		L131		H132	
2	(393)	TT GGA GTG GTC ACC GGC TTG	(HA)	CAT CTT GCT GAA GTA TGT CAC CG	(416)
		L175		S176	
3	(524)	CA GCC ATC GCC ATC AAT CTG CTG	(HA)	TCT GCA GGA AGG GTC CCC CTG TG	(548)
		K201		Y202	
4	(603)	GTG TTT CTT TTT TTG GAC AAA	(HA)	TAT GGC TTG CGG AAG CTG GAA GC	(626)
		P243		S244	
5	(729)	CTC AGG GGC ATG TTC GTG CCG	(HA)	TCC TGT CCA GGG TGC CGC ACC	(750)
5b			(HA) x2		
		A248		N249	
6	(852)	C AAG TCT AGA CAG GTG AAT CGG GCC	(HA)	AAT AAG CAG GAA GTG CGG GAA GC	(875)
		L344		F345	
7			(HA)		
		N403		L404	
8	(1209)	GTC ATG GAG GGA TTC CTG AAC	(HA)	CTA AAA TGG TCG CGC TTT GCC	(1230)
8b			(HA) x2		
		V432		E433	
9	(1296)	C GTC GCT GTC TTC CAG GAT GTG	(HA)	GAG CAC CTA ACG GGG ATG AAT G	(1318)
		S468		E469	
10	(1404)	CA AGC CTG CGG CCA GTG ATG AGT	(HA)	GAG TTT TCC AAT GGA ATA GGC TGG	(1421)
		H504		V505	
11	(1512)	GTT TAT GTC CAG GAG CTA GGG CAT	(HA)	GTG GCA CTC TAT GTG GTG GCT GC	(1532)
11b			(HA) x2		
		K561			
CT	(1660)	GAT ACC AGC GGT GGC AAC ATT AAG	(HA)	TAA AAG CTT CTC GAG ACT G	
(HA)[c] YPYDVPDYAS					

[a] Nucleotide position in sequence of Slc11a2 isoform I. [b] Amino acid residue immediately preceding the site of insertion of the HA epitope. [c] HA epitope sequence.

using lipofectamine 2000 (Invitrogen) as per the manufacturer's instructions. Selection for stably transfected clones was carried out in medium containing G418 (geneticin, 1.4 mg/mL) for 14 days. Individual colonies were then isolated and expanded. LLC-PK1 cell clones stably transfected with the various *Slc11a*-HA/pCB6 constructs were lysed in buffer (50 mM Tris-HCl, pH 8.0, 137 mM NaCl, 1% NP40, 10% glycerol) supplemented with protease inhibitors (1 mM phenylmethanesulfonyl fluoride [PMSF], 1 μM pepstatin, 0.3 μM aprotinin, 1 μM leupeptin). These whole cell extracts were separated by SDS−PAGE, and clones exhibiting high levels of Slc11a2-HA protein expression were identified by immunoblotting, as previously described (*31*), and using affinity-purified rabbit polyclonal anti-mouse Nramp2/DMT1 (1:1000) or a monoclonal mouse anti-HA antibody (1:2000). Secondary anti-rabbit and anti-mouse antibodies conjugated to hoseradish peroxidase were used at 1:20000.

Divalent Metal Transport Assay. Metal transport by individual tagged Slc11a2-HA proteins expressed in transfected LLC-PK1 cell clones was carried out using a fluorescence quenching assay, exactly as we have previously described (*31*). Calcein-AM was prepared as a 500 μM stock solution in dimethyl sulfoxide (DMSO), while ferrous ammonium sulfate (Fe^{2+}) and cobalt chloride (Co^{2+}) were prepared as a 2 mM stock in deionized water. Metal transport in individual LLC-PK1 transfected clones was assessed (initial quenching rates) from fluorescence quenching curves (*31*).

Immunofluorescence. A variation of a cell surface labeling protocol was used to determine the membrane topology of HA tags present in individual recombinant Slc11a2 proteins (*13*). Stable transfectants were grown to confluency on glass coverslips, with empty vector transfected cells serving as a negative control. To localize the HA epitopes expressed on the cell surface (nonpermeabilized conditions), cells were incubated with anti-HA antibody (1:200 dilution) in 2% nonfat milk/DMEM for 2 h at 37 °C prior to fixation with 4% paraformaldehyde in phosphate-buffered saline (PBS) supplemented with 1 mM $MgCl_2$ and 0.1 mM $CaCl_2$ (PBS++), followed by incubation with goat anti-mouse rhodamine-conjugated secondary antibody (1:1000 dilution) in 5% nonfat milk/PBS for 1 h at room temperature. To localize the HA epitopes expressed intracellularly (permeabilized conditions), cells were fixed with 4% paraformaldehyde, followed by permeabilization with 0.1% Triton X-100 for 30 min at room temperature. The cells were then incubated in primary antibody in 5% nonfat milk/PBS for 1 h at room temperature before exposure to secondary antibody as described above. All cells, intact and permeabilized, were incubated in DAPI (4′,6-diamidino-2-phenylindole) for 5 min at room temperature (to stain nuclei) prior to being mounted on glass microscope slides. Cells were visualized with an Axiovert 200 M epifluorescence microscope using a 63× oil immersion objective. Digital images were acquired with a Zeiss AxioCam HRm camera operated with AxioVision 4.3. Images were cropped, assembled, and labeled using Adobe Photoshop 7.0 and Illustrator 10.0 software.

Quantification of Slc11a2-HA Surface Expression. To quantify surface expression of extracellular HA tags (detected by immunofluorescence under nonpermeabilized conditions), we used a colorimetric assay (*36*). For this, 2.0×10^4 cells/well (24-well plastic plates) were allowed to reach confluency, followed by incubation with anti-HA antibody exactly as described for immunofluorescence (omitting the DAPI staining step). The secondary antibody was a horseradish peroxidase (HRP)

conjugated anti-mouse antiserum (1:4000 dilution), and incubation was for 1 h at room temperature in 5% nonfat milk/PBS. The HRP substrate [0.4 mg/mL *o*-phenylenediamine dihydrochloride (OPD); Sigma FAST OPD; 550 μL/well] was used according to the manufacturer's instructions. Absorbance readings (492 nm) were taken in an ELISA plate reader (Bio-Rad Model 450), and background absorbance readings from (i) nonspecific binding of secondary antibody and (ii) nonspecific binding of primary antibody to vector-transfected cells were subtracted for each sample.

Sequence Analyses. Blast analyses using the murine Slc11a2 protein sequence as query were performed to select sequences encoding Slc11 homologues (Blast score >400, full-length % identity >45, expect $<2e^{-110}$) from species representative of Unikonta (motile eukaryotic cells with a single flagellum), such as Amoebozoa and Opisthokonta, comprising Choanozoa (unicellular eukaryote with a flagellum), Fungi, and Metazoa (multicellular motile organisms). The nonmetazoan sequences were used as the phylogenetic outgroup (*37*). The sequences from selected model species were retrieved using NCBI's Entrez life sciences search engine. Unikonta: Amebozoa (*Dictyostelium discoideum*, AAO52395, DdNR2), Opisthokonta: Choanoflagellate (*Monosiga brevicollis*, XP_001750777, MbreNR), Fungi (Zygomycota, *Phycomyces blakesleeanus*, PblNR2), and Metazoa: Porifera (*Reniera*, tropical marine demosponge, ReniNR); Eumetazoa: Cnidaria (*Nematostella vectensis*, sea anemone, XP_001635621, NvecNR) and Bilateria: *Protostomia*: Cuticulata: arthropoda (*Drosophila melanogaster*, Fruit fly, NP_524425 DmeNR, Malvolio) and Lophotrozoa, Platyhelminthe (*Schistosoma mansoni*, AAS99648, SmNRa) and Mollusca (*Mizuhopecten yessoensis*, Giant scallop, BAD99106, MyesNR), *Deuterostomia*: Echinodermata (*Strongylocentrotus purpuratus*, sea urchin, XP_781841, SpurNRa), Chordata (*Ciona intestinalis*, Sea squirt, XP_002127954, CinNR), Vertebrata: Actinopterygii, Teleost fishes (*Pagrus major*, Red seabream, AAR83912, PmaNR, and *Danio rerio*, Zebra fish, NP_001035460, DreNR) Sarcopterygii, Tetrapoda, Amphibia (Frogs) *Xenopus* (*Silurana*) *tropicalis* (NP_001116938, XtrNR2) and *Xenopus laevis* (NP_001088008, XlaeNR1), Amniota, Archosauria (*Gallus gallus*, chicken, ABI24020, GgNR2, and NP_990295.1, GgNR1), Mammalia (*Mus musculus*, laboratory mouse, P49282, MmNR2, P41251, MmNR1). The 18 sequences were aligned using ClustalX (*38*); the multiple sequence alignment was edited manually using Seaview (*39*) and displayed with Genedoc.

Homology Modeling. The mouse Slc11a2 sequence was used as query to generate the best structural models resembling templates present in the PDB using a threading approach, which combines tridimensional fold recognition by sequence alignment with template crystal structures and model structure refining (*40*). Three complementary suites of programs were used: (a) the LOcal MEta-Threading-Server (*41*) that returns the best structure predictions collected from nine independent threading algorithms and ranked using a consensus method; i.e., best models are more frequent and structurally refined using Modeler (*42*); (b) the I-TASSER server (*43*), which uses variations of the threading approach based on sequence profile−profile alignments combined to *ab initio* modeling by iterative implementation of the Threading ASSEmbly Refinement (TASSER); (c) the MUSTER server (*44*) that uses the MUlti-Source ThreadER (MUSTER) to incorporate weighted information from six sources to improve fold recognition and that uses also Modeler for structural refinement. The best models were selected among those predicted by the three approaches, and candidate models were checked for acceptable Cα root-mean-squared deviation (rmsd, <6 Å for template with less than 20% sequence identity with Slc11a2) and consistency between locations modeled for (Slc11 family specific) functional sites and prior experimental results of solvent accessibility *in situ*: MntH TMD1 Asp^{34} and TMD6 His^{211} apparently accessible, and $Asn^{37, 250, 401}$ in TMD1, 7, and 11, not accessible (*27*).

RESULTS

Construction of Epitope-Tagged Slc11a2 Mutants. The multiple sequence alignment presented in Figure 1 shows the position of the TM domains for the animal members of the Slc11 transporter family as predicted by homology threading (*27*). To verify this model as well as establish the position and polarity of individual TMDs, we used an epitope insertion technique previously utilized to establish the membrane topology of several independent ABC transporters (*34*, *45*). This method consists of inserting hemmaglutinin A (HA) epitopes in various extracytoplasmic (EC) and intracytoplasmic (IC) loops delineated by pairs of predicted TMDs, expressing the recombinant proteins in transfected cells and monitoring the polarity of the engineered HA tags by immunofluorescence in intact or permeabilized cells to reveal extra- and intracytoplasmic loops. This approach allows one to obtain topological data in transport-competent proteins properly expressed at the plasma membrane. Additionally, certain HA tag insertions causing loss of transport can provide additional clues on structure−function relationships.

HA epitopes (YPYDVPDYAS) were inserted at both termini and in each predicted loop (from hydropathy plot (*23*)) between pairs of consecutive TMDs (Figures 1 and 2). The insertion positions of the HA epitopes were deliberately chosen as the least conserved regions among Slc11 family members to minimize possible disruptions on protein function (Figure 1). HA epitopes were inserted at positions 1 (N terminus; NT construct), 98 (construct 1), 131 (construct 2), 175 (construct 3), 201 (construct 4), 243 (construct 5a), 284 (construct 6), 344 (construct 7), 403 (construct 8a), 432 (construct 9), 468 (construct 10), 504 (construct 11a), and 561 (C-terminus, CT construct) (Figure 2). In addition, two adjacent HA tags were inserted at positions 243 (5b), 403 (8b), and 504 (11b) to increase the immunofluorescence signal. We used *Slc11a2* isoform I cDNA as the backbone for HA tag insertion as it shows higher surface expression and slower internalization kinetics than isoform II in porcine LLC-PK1 cells (*13*, *36*), facilitating detection of cell surface protein expression by immunofluorescence.

Expression of Epitope-Tagged Slc11a2 Mutants in Transfected LLC-PK1 Kidney Cells. All tagged *Slc11a2* cDNAs were transfected into LLC-PK1 cells, and the expression of the resulting HA-tagged Slc11a2 proteins was verified by immunoblotting. Representative immunoblots using a polyclonal antibody recognizing the N-terminus of Slc11a2 (Figure 3A) and an anti-HA monoclonal antibody (Figure 3B) are shown for single clones. Previous studies in these cells have shown that Slc11a2 is detected as two immunoreactive species of ~60 and ~90 kDa, corresponding to core glycosylated and complex glycosylated forms, respectively (*46*). Briefly, we could obtain stable transfectants expressing robust levels of Slc11a2 for constructs 4−11 as well as for constructs bearing N- and C-termini epitope tags. For constructs 1−3, it was difficult to obtain stably transfected clones expressing robust levels of Slc11a2, and in cell clones positive for expression, only low levels of the

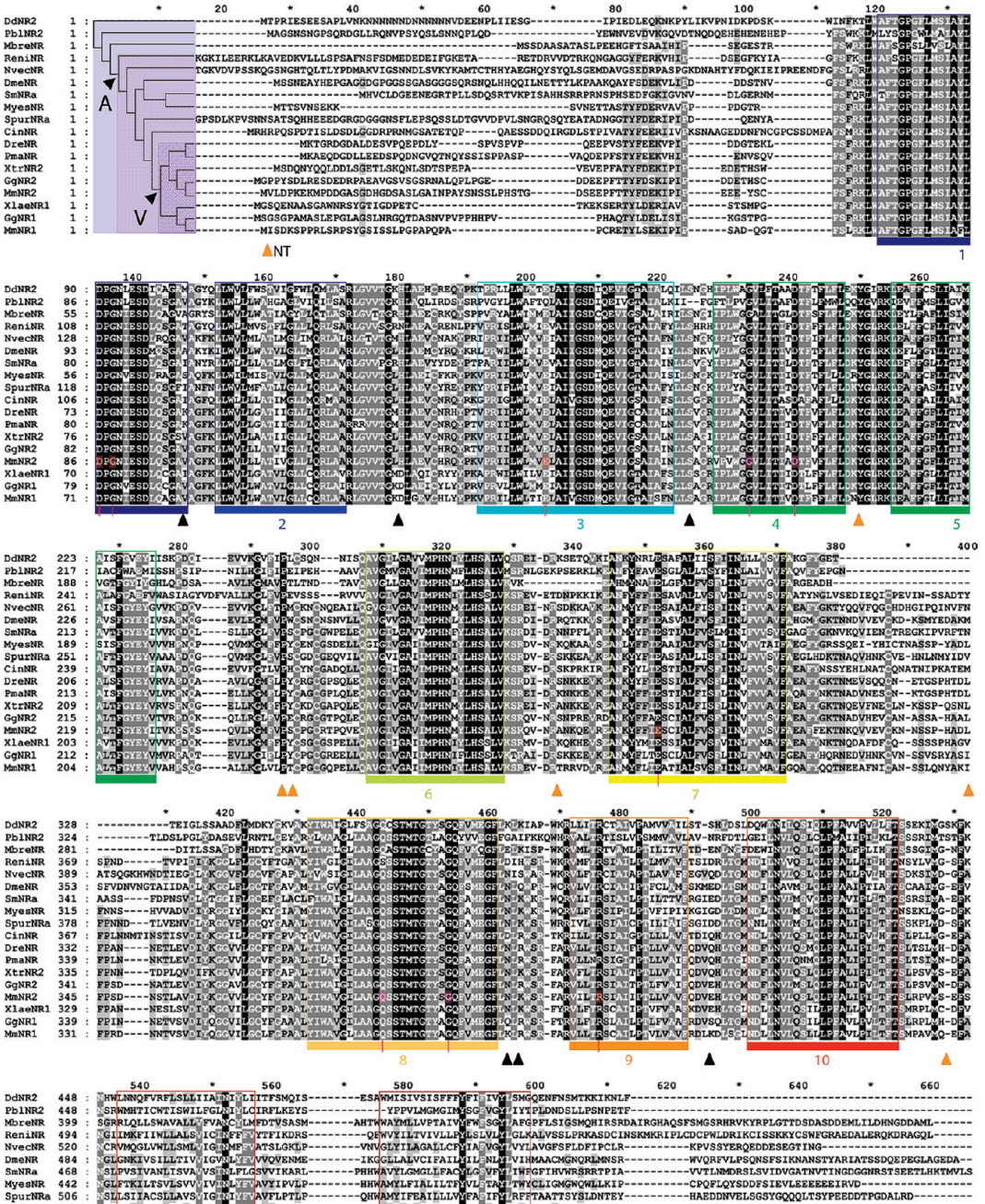

FIGURE 1: Evolutionary conservation of the hydrophobic core of Slc11a2 (TMD1−10). Multiple sequence alignment of Slc11 homologues from representative Unikonta species (phylogenetic relationships schematized and inserted at the beginning of the alignment, A, animals, and V, vertebrates): Amebozoa (DdNR2), Choanoflagellate (MbreNR), Zygomycota (PblNR2) and Metazoa: Porifera (ReniNR) and Eumetazoa: Cnidaria (NvecNR) and Bilateria: *Protostomia*, Cuticulata (DmeNR) and Lophotrozoa, (SmNRa and MyesNR), and *Deuterostomia*, Echinodermata, (SpurNRa), Chordata, (CinNR), Vertebrata, Teleost fishes (PmaNR and DreNR), Tetrapoda, Amphibia (XtrNR2 and XlaeNR1), Amniota (GgNR2 and GgNR1), and Mammalia (MmNR2 and MmNR1). Residue conservation is indicated with three cutoff levels of identity (40%, 80%, and 100%). The position of Slc11a2 transmembrane domains (TMD) was deduced from homology modeling using three different template structures (2a65, LeuT-Slc6 (*53*), 3dh4, vSGLT-Slc5, (*50*) and Mhp1-Slc23 (*51*), and highlighted with rainbow color code (TMD1, blue, TMD12, red). The position of the mouse Nramp2/Slc11a2 (MmNR2) protein used for all studies in this work is the fourth from the bottom of the multiple sequence alignment. The insertion sites for HA epitope tags (triangles) resulting in transport active (orange) or transport inactive (black) Slc11a2 proteins are indicated. The position of critical residues at which mutations are known to cause loss of function (D86, G88, E299, and R416) or to impair severely MmNR2 transport activity (E154, G185, D192, Q384, G394) are indicated in the sequence of MmNR2. They are colored in the primary sequence respectively in red and magenta, and their position is indicated by a tick of the corresponding color under the multiple sequence alignment.

~60 kDa immunoreactive band could be detected (Figure 3A). In addition, expression of constructs 1−3 could only be detected with the anti-Slc11a2 antiserum and not with the anti-HA antibody, suggesting that the HA epitope may be unstable or

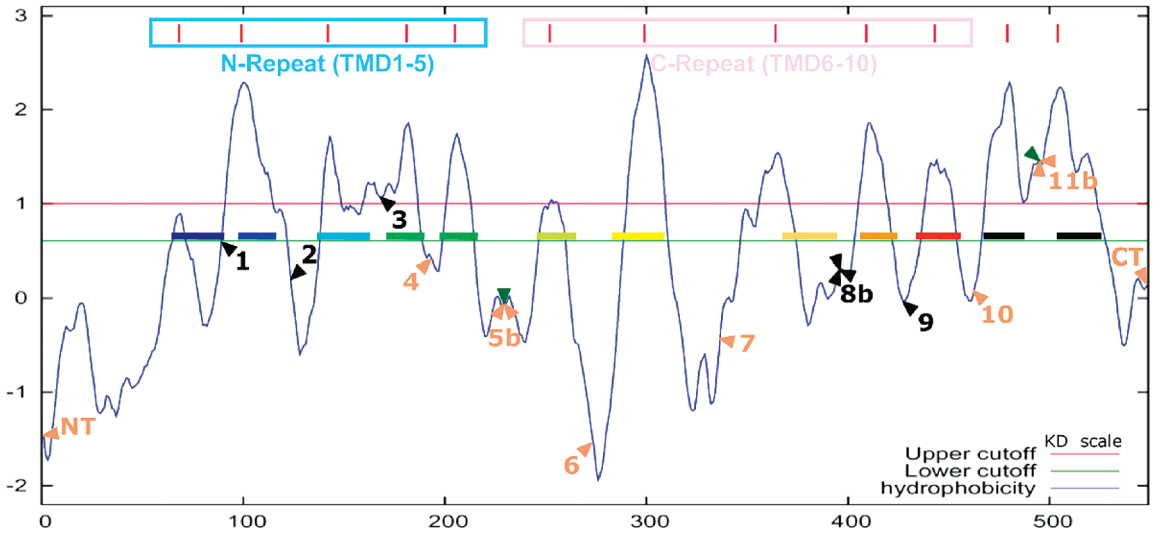

FIGURE 2: Construction of Slc11a2 proteins containing hemagglutinin (HA) epitope tags. The sites for insertion of YPYDVPDYA hemagglutinin (HA) epitopes in individual Slc11a2 proteins are indicated, along with the numerical designation of the construct (NT, 1−11, CT). These have been superimposed on the hydropathy plot of the Slc11a2 protein produced by the TOPPRED software package using a 20-residue long sliding window (core window, 12 residues; wedge windows, 4 residues). The default parameters suggested for predicting the presence of TMDs in eukaryotic proteins were used, such as the Kyte−Doolittle cutoff values (lower, 0.6; putative; upper, 1.0; certain). Orange arrowheads indicate insertion sites that produced functional proteins in which the polarity of the tag could be established by immunofluorescence. Black arrowheads indicate insertion sites that caused partial or complete loss of transport. Single arrowheads represent single epitope tags while double arrowheads (5b, 8b, 11b) represent constructs with two epitope tags inserted side by side. Boxes at the top of the graph indicate the location of the proposed 2-fold structural symmetry in Slc11a2.

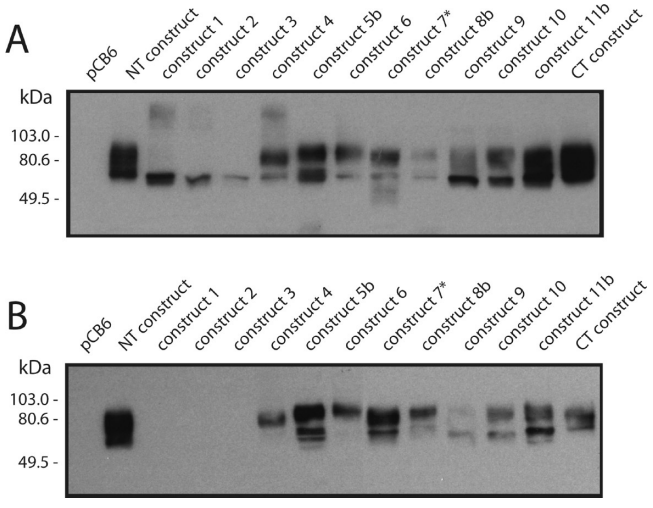

FIGURE 3: Expression of HA epitope-tagged Slc11a2 constructs in LLC-PK1 cells. LLC-PK1 cells were stably transfected with *Slc11a2* isoform I cDNA constructs (listed) modified by the addition of individual or double (b) HA epitopes and inserted in the mammalian expression vector pCB6. Total cell lysates (5 μg per lane) were prepared, resolved by electrophoresis on a 10% SDS−polyacrylamide gel, and analyzed by Western blotting with a polyclonal rabbit anti-Slc11a2 antibody (panel A) or with the mouse monoclonal anti-HA epitope antibody 16B12 (panel B). The asterisk indicates that construct 7 was created by our group in another study (*20*). The positions of the molecular mass markers are indicated on the left of the figure in kDa.

inaccessible for detection in these constructs. These results also suggest that the HA tag insertion in constructs 1−3 may have a detrimental effect on protein stability, maturation, and/or processing to the ~90 kDa fully glycosylated and membrane-expressed isoform.

Functional Analysis of Epitope-Tagged Slc11a2 Mutants in Transfected LLC-PK1 Kidney Cells. To evaluate possible detrimental effects of the HA epitope tag insertions on protein function, transport properties of individual Slc11a2 tagged proteins were assessed in corresponding LLC-PK1 transfected cells (Figure 4). Indeed, proper plasma membrane expression of the protein is required to detect Slc11a2-mediated metal import in intact cells (*24*, *47*). Divalent metal transport activity was measured using a fluorescence quenching assay in calcein-loaded cells (*31*). The pH-dependent transport (pH 5.5) of two divalent metals (Fe^{2+} and Co^{2+}) was tested to assess possible effects of tag insertion on ion selectivity of Slc11a2 (*24*). Transport rates were estimated from the slope of initial quenching curves following addition of metal to the calcein-loaded cells. In these studies, LLC-PK1 cells transfected with empty vectors were used as a negative control, while cells expressing wild-type Slc11a2 were used as a positive control. We noted three phenotypic consequences of tag insertion on Slc11a2 function. For constructs 1−3, HA tag insertion completely abrogated protein function, with transport rates similar to those detected in the pCB6-transfected negative control (no significant difference, $p > 0.05$). These results indicate that this segment of the protein is highly mutation sensitive (affecting either transport *per se* or targeting of the protein to the cell surface), in agreement with results previously obtained with point mutants in these regions (*25*−*27*). In a second group of constructs, namely, 4, 5(b), 6, 7, 10, and 11(b) as well as NT and CT, the epitope insertion had no major functional consequence, with transport rates similar or superior to those detected in the positive control (7−12-fold stimulation above background). Finally, constructs 8b or 9 repeatedly showed severely reduced transport rates, which were not statistically different ($p > 0.05$) from those measured in the negative control. No major effect of HA tag insertion on ion selectivity was detected in any of the constructs that retained detectable metal transport activity. We next proceeded to determine the subcellular location (intra- or extracytoplasmic) of HA epitopes in Slc11a2 variants that retained transport activity. Due

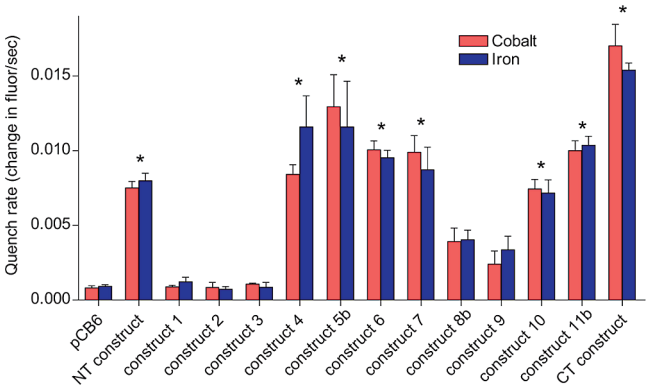

FIGURE 4: Metal transport activity of HA epitope tagged Slc11a2 proteins expressed in LLC-PK1 cells. Metal-transport activity of HA-tagged Slc11a2 variants was tested using a fluorescence-quenching assay. Briefly, 1×10^6 cells were loaded with the metal-sensitive fluorescent dye calcein-AM, followed by incubation with either 20 μM Co^{2+} or 20 μM Fe^{2+} in acidic (pH 5.0) buffer and continuous monitoring of fluorescence quenching over time (2 min) using a spectrofluorometer (excitation wavelength, 488 nm; emission wavelength, 517 nm). The slopes of the initial fluorescence quenching curves were calculated and reflect cation transport activity of individual HA constructs. Results are shown as the initial rates of fluorescence quenching, as described previously (*24*), with error bars representing the standard error on the means of three to five independent experiments. *, one-way ANOVA followed by a Dunnett's *posthoc* test indicated no significant difference ($P > 0.05$) in quench rate between the empty vector control (pCB6) and constructs 1−3, 8, and 9. Furthermore, no significant difference ($P = 0.95$; two-way ANOVA) was observed in quench rate for the two metals tested for any of the clones analyzed.

to the detrimental effect of the tags on Slc11a2 protein expression and metal transport for constructs 1−3, we did not pursue further their characterization.

Membrane Polarity of the Inserted HA-Epitope Tags. The intra- or extracytoplasmic nature of HA tags was determined for each construct by immunofluorescence with their corresponding LLC-PK1 transfectants using the anti-HA monoclonal antibody (Figure 5). Immunofluorescence was performed in parallel on intact cells to detect extracytoplasmic tags and in permeabilized cells treated with detergent to detect intracytoplasmic tags. In all cases, cell nuclei were stained with DAPI to identify the position of the corresponding cells (Figure 5). LLC-PK1 cells transfected with empty pCB6 vector were used as negative controls, and no significant cell-associated fluorescence could be detected in these cells with the anti-HA antibody under either nonpermeabilizing or permeabilizing conditions (Figure 5, panels A−D). In contrast, strong fluorescent signals were observed in both intact and permeabilized cells for constructs 5b (TMD 5−6 segment, two epitopes), 7 (TMD 7−8 segment), 8b (TMD 8−9 segment), and 11b (TMD 11−12 segment, two epitopes) (Figure 5: N, P; V, X; Z, AB; AL, AN), suggesting that the corresponding segments of Slc11a2 are extracytoplasmic. Conversely, strong fluorescence signals were obtained only under permeabilizing conditions for cells transfected with constructs NT (N-terminus), 4 (HA between TMD 4−5 segment), 6 (TMD 6−7 segment), 9 (TMD 9−10 segment), 10 (TMD 10−11 segment), and CT (C-terminus) (Figure 5: F, H; J, L; R, T; AH, AJ; AP, AR), suggesting that the corresponding tagged segments of Slc11a2 are intracytoplasmic. For certain constructs (5, 8, and 11), the insertion of a single HA tag did not produce a clear fluorescence signal in transfected cells in any conditions (data not shown). However, the insertion of a second adjacent HA tag produced unambiguous immunofluorescence results (5b, 8b, and 11b, two epitopes; Figure 5). For all of the constructs, the polarity of the HA tags was validated by immunofluorescence in multiple independently transfected cell clones.

Validation of HA-Epitope Localization in SLC11A2. The topology of inserted HA tags established by immunofluorescence was validated by an enzymatic method, which additionally provides a quantitative measure of exofacial tag surface expression. For this, LLC-PK1 transfectants expressing individual HA-tagged Slc11a2 constructs were fixed and incubated with primary anti-HA antibody with or without prior permeabilization with detergent. The cells were then incubated with a secondary HRP-conjugated antibody, and the amount of bound secondary antibody was quantified colorimetrically using the HRP substrate *o*-phenylenediamine dihydrochloride. Results in Figure 6 show the amount of surface expression (detected under nonpermeabilized conditions) of HA-tagged constructs expressed as a fraction of total protein (detected under permeabilized conditions). LLC-PK1 cells stably transfected with constructs 5b, 7, 8b, and 11b were found to have a significantly greater proportion of accessible HA-tagged Slc11a2 at their surface than constructs NT, 4, 6, 9, 10, and CT (Figure 6). These results are in agreement with immunofluorescence experiments and indicate that the tags in constructs 5b, 7, 8b, and 11b are extracellular while the tags in constructs NT, 4, 6, 9, 10, and CT are intracellular.

A Three-Dimensional Framework for Slc11a2. Homology modeling has recently become an important tool to predict secondary and tertiary structures of membrane proteins. For instance, structural models of the human dopamine transporter DAT were generated using the LeuTAa crystal structure as a template, and these were then used to predict probable primary and secondary pharmacological binding sites on the transporter. Such binding sites were subsequently validated in detailed docking studies with known DAT ligands (*56*). In an independent study, it was noted that the 12 TM helices in the crystal structure of *E. coli* Na^+/H^+ exchanger A (EcNhaA) superimposed strikingly with the pattern of evolutionary conservation of both the bacterial and human Na^+/H^+ exchangers. Homology modeling was then used to assign the position, boundaries, and angulation of the 12 TM domains in the human homologue NHE1 (~10% sequence identity; 14 TMDs in total). This exercise positioned some key residues and functional sites within a predicted highly conserved membrane fold in the human protein which were then validated experimentally in site-directed mutagenesis studies (*57*).

Topology data obtained experimentally were evaluated using a tridimensional framework derived by sequence threading using available structures of distantly related proteins. Current numbers of protein families (> 30% sequence identity) represent a 3-fold excess compared to protein folds (< 20% sequence identity), and a similar trend was reported for membrane proteins with high α-helical content (*49*). Accordingly, despite little amino acid sequence similarity, three cation-driven membrane transporters (Slc23 Mhp1, Slc6 LeuT, and Slc5 vSGLT) exhibit similar structures, including a novel fold for α-helical integral membrane proteins (*50*−*53*). In addition, these structures represent discrete possible steps in cation-driven transport cycle (open to out, open to out-occluded by substrate, open to in). Homology modeling of Slc11a2 showed excellent superimposition on these apparently unrelated templates (Figure 7), implying common architectural features underlying shared mechanistic aspects of membrane transport. The models that are presented in Figure 7 have been

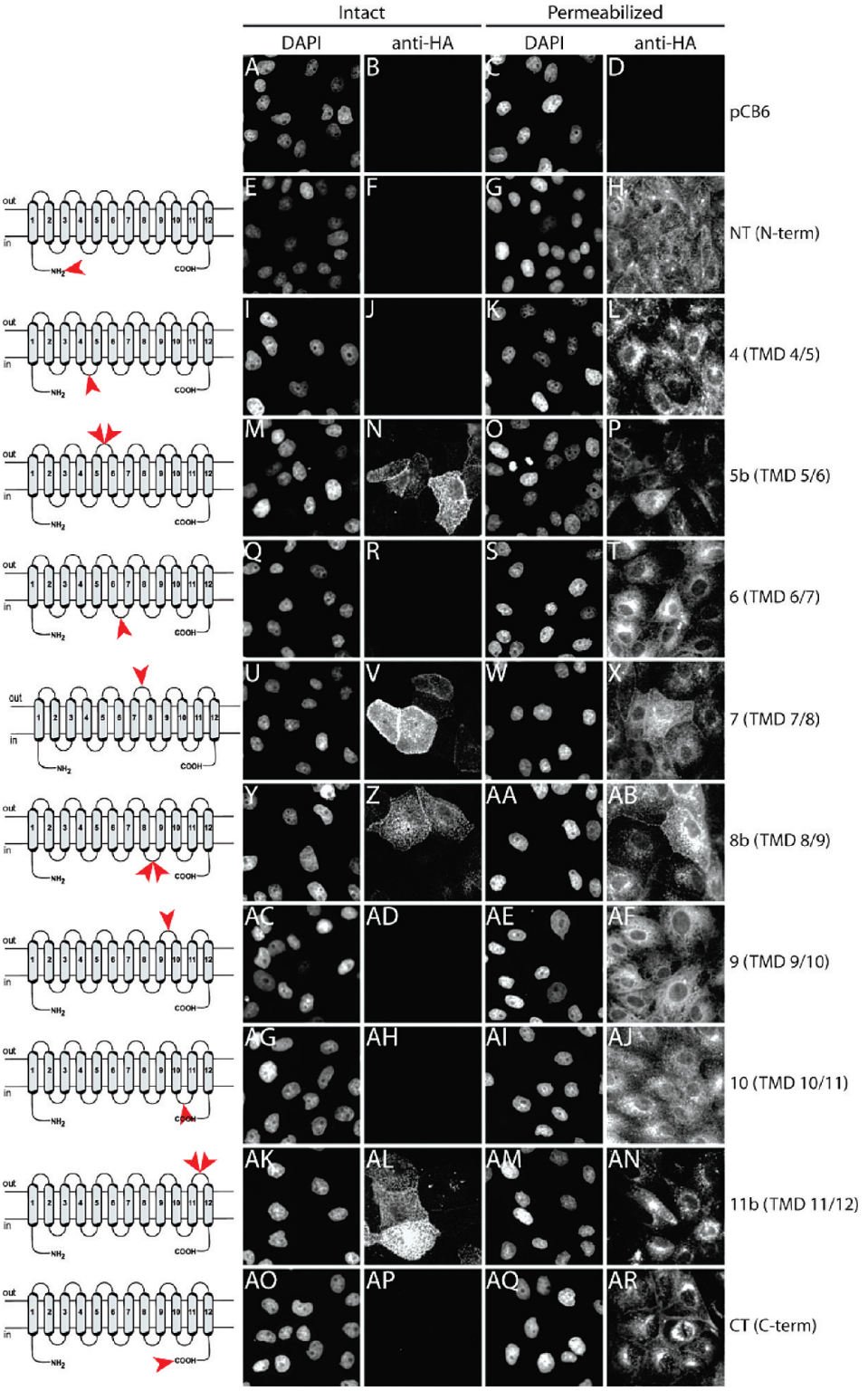

FIGURE 5: Detection of HA epitope-tagged Slc11a2 proteins by immunofluorescence. LLC-PK1 cells stably transfected with either empty pCB6 vector or individual HA-tagged Slc11a2 variants were analyzed by immunofluorescence. A schematic representation of the site of HA tag insertion in Slc11a2 variants is shown in the left panel. Immunofluorescence was carried out with the mouse monoclonal anti-HA epitope antibody 16B12 on cells either untreated (intact cells; left two columns) or pretreated with 0.1% Triton X-100 (permeabilized; right two columns). Cells were then incubated with secondary goat anti-mouse antibody conjugated to rhodamine (Cy3), and images were acquired by epifluorescence microscopy. The HA epitopes in constructs 5b (M-P), 7 (U-X), 8b (Y-AB), and 11b (AK-AN) were detected in intact and permeabilized cells (extracytoplasmic), while the HA epitopes in constructs NT (E-H), 4 (I-L), 6 (Q-T), 9 (AC-AF), 10 (AG-AJ), and CT (AO-AR) were detectable only in permeabilized cells (intracytoplasmic). Nuclear staining (DAPI, columns 1 and 3) was used as a control to ascertain the presence of cells in the microscope field.

highlighted (bold) in Supporting Information Table 1. Models were ranked according to their prediction scores, where higher value increases confidence in the model predicted (taking into account the respective cutoff scores of each program). A compilation of these results is provided in Supporting Information Table 1 together with details regarding the LOMETS predictions

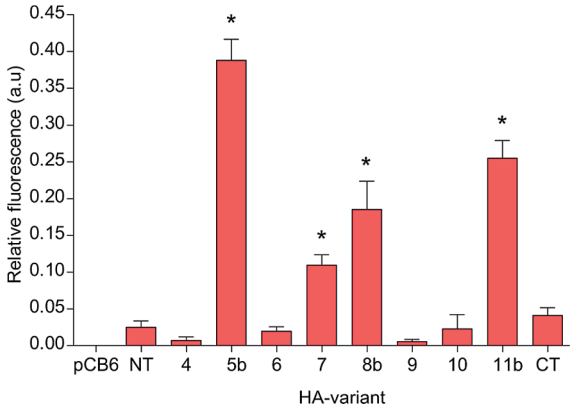

FIGURE 6: Detection of HA epitope-tagged proteins by surface labeling. Stably transfected LLC-PK1 cells were incubated with anti-HA antibody with or without prior detergent (Triton X-100) permeabilization, followed by incubation with a horseradish peroxidase (HRP)-coupled secondary antibody. The amount of bound secondary antibody was determined by a colorimetric assay using *o*-phenylenediamine dihydrochloride (measured at 492 nm). The presence of Slc11a2-HA expressed at the cell surface (in intact cells) is shown as a fraction of total protein expression (in permeabilized cells) normalized for nonspecific binding of primary and secondary antibodies in nontransfected LLC-PK1 cells. Error bars represent standard errors of the means of two independent experiments carried out in duplicate. *, one-way ANOVA followed by a Dunnett's *posthoc* test indicated a significant difference ($P < 0.01$) in cell surface fluorescence between cells transfected with the empty vector control (pCB6) and constructs 5b, 7, 8b, and 11b.

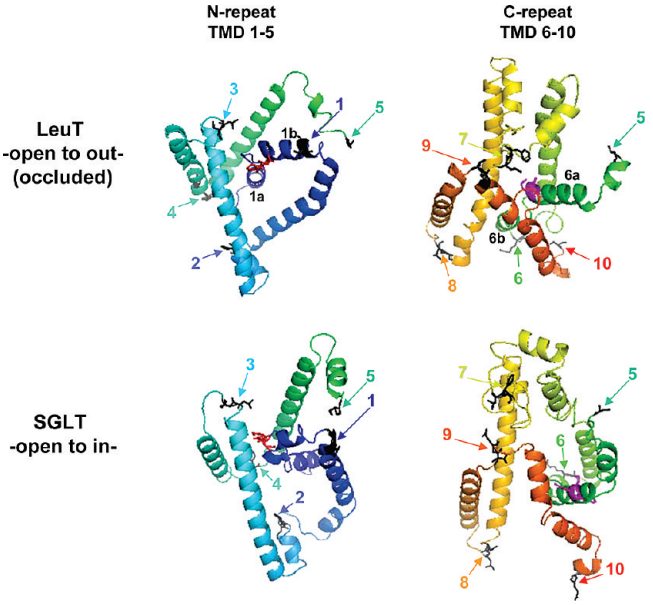

FIGURE 7: Position of HA epitope insertion sites on the predicted structural model of Slc11a2. Slc11a2 models were deduced from homology threading and structure refining based on the crystal structures of LeuT (top) and vSGLT (bottom). These may represent discrete steps in the translocation cycle (open to outside/occluded and open to inside, respectively) of a structural fold shared by different families (e.g., Slc 5, 6, and 23). The view is presented from the external surface (outside). For clarity, the predicted 10 TMD forming the hydrophobic core of Slc11a2 has been split at site 5 to present the N- and C- terminal halves juxtaposed horizontally and comprising respectively TMD1−5 (blue to green) and TMD6−10 (green to orange). The Slc11-specific functional motifs Asp-Pro-Gly and Met-Pro-His (*27*) are highlighted in red and magenta, and their respective locations between TMD1a/b and TM6a/b are indicated in the LeuT model (top). The side chains of the amino acids flanking each insertion site (numbered according to the preceding TMD) are highlighted in black. Comparison of the top and bottom panels shows possible movements that may facilitate substrate uptake (N-domain, TMDs 1, 2, and 5, and C-domain, TMDs 6, 7, and 10). Details on the models presented in Figure 7 are provided in Supporting Information Tables 1 and 3.

which are given in Supporting Information Table 2. Similar results were obtained using different approaches (mGenTHREADER, GenTHREADER, CBS WWW Server) (data not shown). Models for the open-to-out form (resembling LeuT and Mhp1), and for the open-to-in form (vSGLT) were frequently obtained with significant scores. Although the models obtained with the template LeuT had lower confidence values, their architecture was highly consistent with those derived from both Mhp1 and vSGLT templates. Finally, the models presented were selected for consistency with additional functional data published by our group. To evaluate accuracy in modeling the Slc11a2 fold, we used a representative set of candidate models that comprised the top four candidate structures produced by the program MUSTER, which represent either the LeuT/vSGLT/Mhp1 fold or the GlpT/MFS fold (Supporting Information Table 1). These models were checked for acceptable Cα root-mean-squared deviation (rmsd) using three different programs that perform pairwise structure alignment and provide a global rmsd. Each model was aligned both with its respective template and with a fourth template that also fits the LeuT/vSGLT/Mhp1 fold (BetP). The results presented in Supporting Information Table 3 demonstrate excellent superposition of each model structure with its respective template and show that models representing the LeuT fold superimpose better on the BetP template than a MFS model. Notably, the most conserved elements of the Slc11 hydrophobic core (TMD1, 3, 6, and 8; Figure 1) correspond to TMDs that play key roles in the cation-driven membrane transport mechanism (*50*−*53*) (Figure 7).

The Slc11a2 tridimensional models derived from Mhp1, LeuT, and SGLT were used to locate residues at which naturally occurring and experimentally induced point mutations abrogate SLC11A2 transport activity in mice and humans. These mutations were found to affect symmetric elements situated in the same region of the predicted fold: three map to long TMD3 (E154) and TMD8 (Q384, G394), and the mutations causing anemia in mammals affect the adjacent TMD4 and 9 (G185, R416, Supporting Information Figure 1). Such structure−function relationships support the structural model we propose for Slc11a2, including a long and oblique arrangement for TMD3 and 8 (Figure 7 and Supporting Information Figure 2). Additional mutations detrimental for Slc11a2 affect other parts of the molecule that are predicted to be mobile during the transport cycle (respectively TMD1 and 7 and TMD2 and 5, Supporting Information Figures 1 and 2). The tridimensional localization of critical Slc11a2 mutations provides circumstantial support for the proposed structural model. Thus, our experimental results with inserted HA tags in intact cells, including their effects on transport, can be discussed, taking into consideration this structural and functional framework.

DISCUSSION

We have used epitope tagging to map the position and polarity of individual TMD of the Slc11a2 metal transporter. This approach consists of inserting HA tags at sites showing relatively low sequence conservation and delineating TMD segments predicted by hydropathy profiling and other computational tools (Figures 1 and 2). The recombinant, HA-tagged proteins are

stably expressed and tested functionally in mammalian cells, where the polarity of the tag is established by immunofluorescence (Figure 5) in intact (extracytoplasmic) vs permeabilized cells (intracytoplasmic). The experimental results are then evaluated using candidate tridimensional models obtained by sequence threading using available structures in the PDB database. This approach provides several advantages over mapping techniques using truncated proteins fused to indicator genes and proteins (*32*, *48*). Indeed, topology data obtained by epitope mapping are with functional proteins that are properly processed and inserted in the membrane of intact cells in a transport-competent state. By the same token, topology data obtained from HA-tagged proteins showing altered transport function must be interpreted with great caution. Analyses of sequence threading and motif conservation are useful for this purpose; for instance, tag insertions impairing Slc11a2 activity were found mostly in (a) short loops connecting conserved TMDs (constructs 1, 3, 8b, and 9), (b) the group of five positive charges that are conserved in the 15 residue stretch spanning the loop between TM8−9, and (c) the N-end of TMD9 which may contain a topogenic (positive-inside) signal. Thus, epitope insertions that impair transport activity may point to protein segments that are essential for proper structure, membrane arrangement, and function of the proteins and that may be studied by further mutagenesis.

Constructs NT, 4, 5b, 6, 7, 10, 11b, and CT were transport active and showed unambiguous polarity in immunofluorescence studies being either intracytoplasmic (NT, 4, 6, 10, CT), or extracytoplasmic (5b, 7, 11b). This demonstrates that the N-terminus, the C-terminus, and the protein segments separating TM4−5, TM6−7, and TM10−11 are intracytoplasmic. On the other hand, the segments separating TM5−6, TM7−8, and TM11−12 can be unambiguously assigned as extracellular. These results are in agreement with structural models deduced from sequence profiling and modeling (Figures 1 and 2) but also with topology data obtained for the distant bacterial Slc11 relative MntH (*32*). Genetic fusions of cytoplasmic or periplasmic reporter proteins at different locations in MntH suggested that loops 1/2, 5/6, 7/8, and 9/10 and the C-terminus are periplasmic while loops 2/3, 6/7, 8/9, and 10/11 are cytoplasmic. Also, both the C-terminus and the segment separating TMD7 and 8 were shown to be periplasmic in transport-active MntH. These and additional data suggested an 11 TMD topology model, where the MntH N-terminus is cytoplasmic and the C-terminus periplasmic, which was consistent with computer-based predictions based on hydrophobicity, secondary structure propensity, conservation, and charge density (*32*).

On the other hand, no topology data could be obtained for Slc11a2 protein segments delineated by the TM1−2, TM2−3, and TM3−4 intervals and represented by HA tag insertions in constructs 1−3. For these constructs, we were unable to isolate stable LLC-PK1 transfectants expressing high levels of the corresponding proteins despite several attempts. Positive clones only showed low level expression of a protein isoform (~60 kDa) that corresponds to the immature form of Slc11a2. We interpret this result as epitope insertion in this portion of the protein causing improper maturation and processing of the protein (retention in the endoplasmic reticulum), preventing functional insertion in the membrane as determined by the absence of an immunofluorescence signal in transfected cells (data not shown) and ultimately leading to absence of detectable transport. The mutation-sensitive nature of this region of Slc11a2 has been previously noted in parallel mutagenesis experiments (*25*). Complementation studies in yeast *Smf* mutants and electrophysiological measurements in *Xenopus* oocytes showed that the highly conserved C-terminal portion of predicted TMD1 and the N-terminal portion of predicted TMD2 are critical for transport. These studies established the importance of several residues in substrate specificity (including G119, D124, and Q126) and established a critical role for the G88 residue found in the invariant DPGN motif in this region (*25*, *28*). Finally, the parallel mutational studies of positions D93 and Q95 and of the DPGN motif from the MntH bacterial relative have led to the proposal that this region of TM1-TM2 may form part of a metal binding site in the protein (*26*, *27*, *54*). The LeuT structural model (*52*, *53*) suggests a pseudo-2-fold symmetry, in which TMDs 1 and 6 contain membrane spanning discontinuous helices involved in substrate recognition and ion binding (Figure 7). Such a critical role for TMD1 could help to explain the loss of function mutation of Slc11a2 construct 1, which bears an HA tag insertion immediately C-terminal to TMD1. Likewise, the crystal structure of LeuT reveals substantial secondary structure in the hydrophilic loops between TMDs 2−4 and 7−8, loops implicated in conformational changes during substrate transport (*52*, *53*). Therefore, it is tempting to speculate that disruption of such short α-helices (possibly conserved in Slc11a2) may also explain the loss of protein stability, maturation, and/or transport noted for constructs 2 and 3 bearing HA epitopes in these segments.

Constructs 8b (insertion in TM8−9 segment, position 403) and 9 (insertion in TM9−10 segment, position 432) gave ambiguous results that warrant additional discussion. In transfected LLC-PK1 cells, these epitopes were accessible to the anti-HA antibody and could be mapped to the extracytoplasmic and intracytoplasmic face of the membrane, respectively. However, this localization does not agree either with the topological model proposed by hydropathy profiling (Figures 1 and 2) and that is supported by topology mapping in other functional HA tagged constructs, nor with the proposed membrane structure of the distant bacterial MntH relative (*27*, *32*), nor with the structural model obtained by threading and homology mapping (Figure 7 and Supporting Information Figures 1 and2). Interestingly, the corresponding Slc11a2 constructs 8b and 9 showed considerably reduced transport activity, indicating that the tag insertion disrupted one or more structural and/or functional properties of the two variants. Therefore, we cannot exclude the possibility that tag insertion in these constructs disrupted normal topology or membrane insertion of the proteins leading to (a) reduced transport activity and (b) aberrant exposure of the HA epitope and erroneous associated topology data. Finally, hydropathy predictions used to derive secondary structure models (Figure 2) are largely based on the presumption that most TMDs lie perpendicularly to the plane of the membrane and consist of approximately 19 or 20 amino acids. This assumption may not be valid for all TMDs. TMDs 3 and 8 in the transporters LeuT and Mhp1 and their counterparts TMDs 4 and 9 in SGLT consist of 30 or more amino acids. They span the membrane at oblique angles and appear to tilt around a central axis parallel to the membrane plane, suggesting that their extremities may alternatively be exposed to the membrane hydrophobic core and/or be engaged in interhelical contacts during transport (*50*, *51*, *53*)-(Supporting Information Figure 2). Any epitope insertion near the boundaries of such long TMD would obviously compromise topology and function. Additional epitope mapping experiments with other epitope tags inserted in neighboring positions will be required to formally test this hypothesis.

Regarding HA tag 8b, such a double tag could, on the one hand, weaken the topogenic signal that precedes TMD9 by dissipating the net positive charge of this hydrophilic segment and preventing correct positioning relative to the translocon machinery and the cytoplasmic side of the membrane. On the other hand, this effect might be amplified by the peculiar conformation of TMD8, which is modeled forming an angle close to 45 deg with the membrane plane and likely interacting with other helices (Figure 7). Therefore, HA tag insertion immediately downstream of N403 (in construct 8b) may indeed be detrimental to function. This fourth predicted intracellular loop of Slc11a2 (targeted in construct 8b) follows a segment highly conserved among Slc11 orthologues, including a mutation-sensitive and highly conserved 20 amino acid sequence motif (positions 384−403). This conserved sequence motif shows that many invariant residues and mutations at several of these sites significantly reduce or completely abrogate transport (*26*, *28*). Likewise, the insertion of an HA epitope tag in the corresponding segment of the yeast orthologue SMF1 also caused a loss of function (*55*). But whether this highly conserved sequence motif forms a membrane-reentrant loop following TMD8 or is instead integral to a longer TMD8 as currently suggested by homology modeling (Figure 7) remains to be clarified.

The results yielded by the apparently symmetric constructs 4 and 9 were somewhat unexpected given the levels of sequence conservation observed at the corresponding sites. Modification of the well-conserved loop separating TM4−5 did not alter Slc11a2 functional expression, providing unambiguous data in a region that had not been previously probed in any Slc11 members. In contrast, insertion of the HA tag in the moderately conserved loop separating TM9−10 may have impaired membrane insertion of TMD9. This TMD is short comparatively to others, and it has a positively charged amino end. Insertion of two negative charges (from the HA tag) close to the carboxyl end of TMD9 may further reduce the overall hydrophobicity of that TMD, resulting in less effective membrane partitioning and preventing proper overall membrane insertion. Also, based on the role in external gating of the translocation pathway that was reported for TMD10 (Figure 7, C-repeat, compare the LeuT and vSGLT conformations), another possible explanation is that HA tag insertion at site 9 may impede a conformational change in Slc11a2 that may be critical for transport function.

We have also used the sequence of constructs 1, 2, 3, 7, 8b, 9, and 10 as queries for threading and homology modeling (data not shown). These analyses showed that epitope tagging at sites experimentally observed to severely affect protein function had a marked effect on homology modeling (e.g., much lower score prediction compared to wild-type Nramp2 for construct 1 < construct 8b < construct 2 ~ construct 9). These results confirm that epitope insertions at these sites may have functional consequences on membrane insertion and transport activity of the corresponding Slc11a2 variants, and therefore topology results with these constructs (namely, 8b and 9) must be interpreted with caution.

Finally, the structural model we propose for Slc11a2 (and other members of the Slc11 family) only emcompasses 10 of the 12 TM domains of the protein. The core 10 TM domains constitute the functional unit of this family of transporters. TM domains 1−10 (a) are present in all Slc11 relatives and (b) show the highest degree of similarity across relatives, including the presence of highly conserved and functionally critical charged residues (*16*). Although they all function by the same H^+-dependent mechanism and display similar substrate specificity and kinetic parameters, most microbial relatives (bacteria, yeast) have an additional 11th TM, while the higher eukaryote transporters (including Nramp2/Slc11a2) contain 12 TMs. The role of the 11th and 12th TMs and additional C-terminal sequences in the mechanism or regulation of transport is not fully understood. One can speculate that these TM domains may (a) contribute additional functional determinants involved in regulation of transport, (b) provide docking sites for homo- or heterodimerization of the transporter or interaction with other proteins or other membrane constituents, or (c) provide structural determinants for stability and/or targeting to specific membrane microdomains. With respect to the latter point, we have previously shown that several sequence determinants downstream of TM12 at the C-terminus play an important role in targeting Slc11a1 and Slc11a2 to different endomembrane compartments and recycling from the plasma membrane via recycling endosomes (*6*, *29*, *37*).

Together, our results on Slc11a2 transmembrane topology have not only contributed to validate the structural model obtained by homology threading and modeling but additionally provide a structural framework for structure−function studies in this family of transporters.

ACKNOWLEDGMENT

The authors are indebted to the McGill Imaging Facility for the use of confocal microscopes.

SUPPORTING INFORMATION AVAILABLE

A description of the different conformations of Slc11a2 based on homology modeling, including the projected position of critical residues known to be essential for transport. This material is available free of charge via the Internet at http://pubs.acs.org.

REFERENCES

1. Courville, P., Chaloupka, R., and Cellier, M. F. M. (2006) Recent progress in structure-function analyses of Nramp proton-dependent metal-ion transporters. *Biochem. Cell. Biol. 84*, 960–978.
2. Cellier, M. F., Courville, P., and Campion, C. (2007) Nramp1 phagocyte intracellular metal withdrawal defense. *Microbes Infect. 9*, 1662–1670.
3. Gruenheid, S., Pinner, E., Desjardins, M., and Gros, P. (1997) Natural resistance to infection with intracellular parasites: The Nramp1 protein is recruited to the membrane of the phagosome. *J. Exp. Med. 185*, 717–730.
4. Canonne-Hergaux, F., Calafat, J., Cellier, M., Grinstein, S., Borregaard, N., and Gros, P. (2002) Expression and subcellular localization of Nramp1 in human neutrophil granules. *Blood 100*, 268–275.
5. Jabado, N., Jankowsky, A., Dougaparsad, S., Picard, V., Grinstein, S., and Gros, P. (2000) Natural resistance to intracellular infections: Nramp1 functions as a pH-dependent manganese transporter at the phagosomal membrane. *J. Exp. Med. 192*, 1237–1248.
6. Jabado, N., Cuellar-Mata, Grinstein, S., and Gros, P. (2003) Iron chelators mimic the Nramp1 effect on the maturation of salmonella vacuole in macrophages lacking functional Nramp1. *Proc. Natl. Acad. Sci. U.S.A. 100*, 6127–6132.
7. Huynh, C., and Andrews, N. W. (2008) Iron acquisition within host cells and the pathogenicity of *Leishmania*. *Cell Microbiol. 10*, 293–300.
8. Malik, S., Abel, L., Tooker, H., Poon, A., Simkin, L., Girard, M., Adams, G. J., Starke, J. R., Smith, K. C., Graviss, E. A., Musser, J. M., and Schurr, E. (2005) Alleles of the NRAMP1 gene are risk factors for pediatric tuberculosis disease. *Proc. Natl. Acad. Sci. U.S.A. 102*, 12183–8.
9. Poon, A., and Schurr, E. (2004) The *NRAMP* genes and human susceptibility to common diseases, in The Nramp Family (Cellier, M., and Gros, P., Eds.) pp 29−43, Kluwer Academic Plenum Publishers, New York, NY.

10. Canonne-Hergaux, F., Gruenheid, S., Ponka, P., and Gros, P. (1999) Cellular and sub-cellular localization of the Nramp2 iron transporter in the intestinal brush border and regulation by iron. *Blood 93*, 4406–4417.
11. Canonne-Hergaux, F., Fleming, M., Levy, J., Gauthier, S., Andrews, N., and Gros, P. (2000) Increased expression and inappropriate targeting of the DMT1/Nramp2 iron transporter at the intestinal brush border of microcytic anemia *mk* mice. *Blood 96*, 3964–3970.
12. Hentze, M. W., Muckenthaler, M. U., and Andrews, N. C. (2004) Balancing acts: molecular control of mammalian iron metabolism. *Cell 117*, 285–297.
13. Lam-Yuk-Tseung, S., and Gros, P. (2006) Distinct targeting and recycling properties of two isoforms of the iron transporter DMT1 (Nramp2, Slc11a2). *Biochemistry 45*, 2294–301.
14. Fleming, M. D., Romano, M. A., Su, M. A., Garrick, L. M., Garrick, M. D., and Andrews, N. C. (1998) Nramp2 is mutated in the anemic Belgrade (b) rat: evidence of a role for Nramp2 in endosomal iron transport. *Proc. Natl. Acad. Sci. U.S.A. 95*, 1148–1153.
15. Fleming, M. D., Trenor, C. C., Su, M. A., Foernzler, D., Beier, D. R., Dietrich, W. F., and Andrews, N. C. (1997) Microcytic anemia mice have a mutation in Nramp2, a candidate iron transporter. *Nat. Genet. 16*, 383–386.
16. Iolascon, A., d'Apolito, M., Servedio, V., Cimmino, F., Piga, A., and Camaschella, C. (2005) Microcytic anemia and hepatic iron overload in a child with compound heterozygous mutations in DMT1 (SLC11A2). *Blood 107*, 349–354.
17. Beaumont, C., Delaunay, J., Hetet, G., Grandchamp, B., de Montalbert, M., and Tchernia, G. (2006) Two new human *DMT1* gene mutations in a patient with microcytic anemia, low ferritinemia, and liver iron overload. *Blood 107*, 4168–4170.
18. Mims, M. P., Guan, Y., Pospisilova, D., Priwitzerova, M., Indrak, K., Ponka, P., Divoky, V., and Prchal, J. T. (2005) Identification of a human mutation of DMT1 in a patient with microcytic anemia and iron overload. *Blood 105*, 1337–1342.
19. Lam-Yuk-Tseung, S., Camaschella, C., Iolascon, A., and Gros, P. (2006) A novel R416C mutation in human DMT1 (Slc11a2) displays pleiotropic effect on function and causes microcytic anemia and hepatic iron overload. *Blood Cells Mol. Dis. 36*, 347–354.
20. Forbes, J., and Gros, P. (2003) Iron and manganese transport by Nramp1 (*Slc11a1*) and Nramp2 (*Slc11a2*) expressed at the plasma membrane. *Blood 102*, 1884–1892.
21. Mackenzie, B., Ujwal, M. L., Chang, M. H., Romero, M. F., and Hediger, M. A. (2006) Divalent metal-ion transporter DMT1 mediates both H^+ coupled Fe^{2+} and uncoupled fluxes. *Pfuegers Arch. 451*, 544–558.
22. Gunshin, H., Mackenzie, B., Berger, U. V., Gunshin, Y., Romero, M. F., Boron, W. F., Nussberger, S., Gollan, J. L., and Hediger, M. A. (1997) Cloning and characterization of a mammalian proton-coupled metal-ion transporter. *Nature 388*, 482–488.
23. Cellier, M., Prive, G., Belouchi, A., Kwan, T., Rodrigues, V., Chia, W., and Gros, P. (1995) The natural resistance associated macrophage protein (Nramp) defines a new family of membrane proteins conserved throughout evolution. *Proc. Natl. Acad. Sci. U.S.A. 92*, 10089–10094.
24. Lam-Yuk-Tseung, S., Govoni, G., and Gros, P. (2003) Mutational analysis of conserved membrane charges reveals altered pH dependence of metal transport by DMT1 mutants lacking conserved histidines in TM6. *Blood 101*, 3699–3707.
25. Cohen, A., Nevo, Y., and Nelson, N. (2003) The first external of the metal ion transporter DCT1 is involved in metal ion binding and specificity. *Proc. Natl. Acad. Sci. U.S.A. 100*, 10694–10699.
26. Chaloupka, R., Courville, P., Veyrier, F., Knudsen, B., Tompkins, T. A., and Cellier, M. F. (2005) Identification of functional amino acids in the Nramp family by a combination of evolutionary analysis and biophysical studies of metal and proton co-transport in vivo. *Biochemistry 44*, 726–733.
27. Courville, P., Ubankova, E., Rensing, C., Chaloupka, R., Quick, M., and Cellier, M. F. M. (2008) Solute carrier 11 cation symport requires distinct residues in transmembrane helices 1 and 6. *J. Biol. Chem. 283*, 9651–9658.
28. Pinner, E., Gruenheid, S., Raymond, M., and Gros, P. (1997) Functional complementation of the yeast divalent cation transporter family SMF by a member of the mammalian natural resistance associated macrophage family, Nramp2. *J. Biol. Chem. 272*, 28933–28938.
29. Cooper, C. A., Shayeghi, M., Techau, M. E., Capdevila, D. M., MacKenzie, S., Durrant, C., and Bury, N. R. (2007) Analaysis of the rainbow trout solute carrier 11 family reveals iron import < 7.4 and a functional isoform lacking transmembrane domains 11 and 12. *FEBS Lett. 581*, 2599–2604.
30. Vidal, S. M., Pinner, E., Lepage, P., Gauthier, S., and Gros, P. (1996) Natural resistance to intracellular infections: *Nramp1* encodes a membrane phosphoglycoprotein absent in macrophages from susceptible ($Nramp1^{D169}$) mouse strains. *J. Immunol. 157*, 3559–3568.
31. Picard, V., Govoni, G., Jabado, N., and Gros, P. (2000) Functional Analysis Of Mammalian Nramp2 In Intact Cells By A Calcein Quenching Assay. *J. Biol. Chem. 275*, 35738–35745.
32. Courville, P., Chaloupka, R., Veyrier, F., and Cellier, M. F. M. (2004) Determination of transmembrane topology of the *Escherichia coli* natural resistance associated macrophage protein (Nramp) ortholog. *J. Biol. Chem. 279*, 3318–3326.
33. Kuhn, D. E., Lafuse, W. P., and Zwilling, B. S. (2001) Iron transport into mycobacterium avium-containing phagosomes from an Nramp1-(Gly169)-transfected RAW264.7 macrophage cell line. *J. Leukocyte Biol. 69*, 43–49.
34. Kast, C., and Gros, P. (1997) Topology mapping of the amino terminal half of multidrug resistance-associated protein by epitope insertion and immunofluorescence. *J. Biol. Chem. 272*, 26479–26487.
35. Hull, R. N., Cherry, W. R., and Weaver, G. W. (1976) The origin and characteristics of a pig kidney cell strain, LLC-PK. *In Vitro 12*, 670–677.
36. Lam-Yuk-Tseung, S., Touret, N., Grinstein, S., and Gros, P. (2005) The carboxyl terminal domain of DMT1 (Slc11a2) mediates internalization from the cell surface. *Biochemistry 44*, 12149–12159.
37. Lecointre, G., Le Guyader, H., Visset, D., and McCoy, K., Eds. (2006) The tree of life: a phylogenetic classification , Belknap Press of Harvard University Press, Cambridge, MA.
38. Thompson, J. D., Gibson, T. J., and Higgins, D. G. (2002) Multiple sequence alignment using ClustalW and ClustalX, Curr. Protoc. Bioinf., Chapter 2, Unit 2.3.
39. Galtier, N., Gouy, M., and Gautier, C. (1996) SEAVIEW and PHYLO_WIN: two graphic tools for sequence alignment and molecular phylogeny. *Comput. Appl. Biosci. 12*, 543–548.
40. Zhang, Y. (2008) Progress and challenges in protein structure prediction. *Curr. Opin. Struct. Biol. 18*, 342–348.
41. Wu, S., and Zhang, Y. (2007) LOMETS: a local meta-threading-server for protein structure prediction. *Nucleic Acids Res. 35*, 3375–3382.
42. Eswar, N., Webb, B., Marti-Renom, M. A., Madhusudhan, M. S., Eramian, D., Shen, M. Y., Pieper, U., and Sali, A. (2007) Comparative protein structure modeling using MODELLER, Curr. Protoc. Protein Sci., Chapter 2, Unit 2.9.
43. Zhang, Y. (2008) I-TASSER server for protein 3D structure prediction. *BMC Bioinf. 9*, 40.
44. Wu, S., and Zhang, Y. (2008) MUSTER: Improving protein sequence profile-profile alignments by using multiple sources of structure information. *72*, 547–566.
45. Kast, C., Canfield, V., Levenson, R., and Gros, P. (1996) Transmembrane organization of mouse P-glycoprotein determined by epitope insertion and immunofluorescence. *J. Biol. Chem. 271*, 9240–9248.
46. Touret, N., Martin-Orozco, N., Paroutis, P., Furuya, W., Lam-Yuk Tseung, S., Forbes, J., Gros, P., and Grinstein, S. (2004) Molecular and cellular mechanisms underlying iron transport deficiency in microcytic anemia. *Blood 104*, 1526–1533.
47. Lam-Yuk-Tseung, S., Picard, V., and Gros, P. (2006) Identification of a tyrosine-based motif (YSGI) in the amino terminus of Nramp1 (Slc11a1) that is important for lysosomal targeting. *J. Biol. Chem. 281*, 31677–31688.
48. Manoil, C. (1991) Analysis of membrane protein topology using alkaline phosphatase and beta-galactosidase gene fusions. *Methods Cell. Biol. 34*, 61–75.
49. Granseth, E., Seppälä, S., Rapp, M., Daley, D. O., and Von Heijne, G. (2007) Membrane protein structural biology—how far can the bugs take us?. *Mol. Membr. Biol. 24*, 329–332.
50. Faham, S., Watanabe, A., Besserer, G. M., Cascio, D., Specht, A., Hirayama, B. A., Wright, E. M., and Abramson, J. (2008) The crystal structure of a sodium galactose transporter reveals mechanistic insights into Na^+/sugar symport. *Science 321*, 810–814.
51. Weyand, S., Shimamura, T., Yajima, S., Suzuki, S., Mirza, O., Krusong, K., Carpenter, E. P., Rutherford, N. G., Hadden, J. M., O'Reilly, J., Ma, P., Saidijam, M., Patching, S. G., Hope, R. J., Norbertczak, H. T., Roach, P. C., Iwata, S., Henderson, P. J., and Cameron, A. D. (2008) Structure and molecular mechanism of a nucleobase-cation-symport-1 family transporter. *Science 322*, 709–713.

52. Singh, S. K., Piscitelli, C. L., Yamashita, A., and Gouaux, E. (2008) A competitive inhibitor traps LeuT in an open-to-out conformation. *Science 322*, 1655–1661.
53. Yamashita, A., Singh, S. K., Kawate, T., Jin, Y., and Gouaux, E. (2005) Crystal structure of a bacterial homologue of Na^+/Cl^- dependent neurotransmitter transporters. *Nature 437*, 215–223.
54. Haemig, H. A., and Brooker, R. J. (2004) Importance of conserved acidic residues in MntH, the Nramp homolog of *Escherichia coli*. *J. Membr. Biol. 201*, 97–107.
55. Nevo, Y., and Nelson, N. (2006) The Nramp family of metal-ion transporters. *Biochim. Biophys. Acta 1763*, 609–620.
56. Indarte, M., Madura, J. D., and Surratt, C. K. (2008) Dopamine transporter comparative molecular modeling and binding site prediction using the LeuT(Aa) leucine transporter as a template. *Proteins 70*, 1033–1046.
57. Landau, M., Herz, K., Padan, E., and Ben-Tal, N. (2007) Model structure of the Na^+/H^+ exchanger 1 (NHE1): functional and clinical implications. *J. Biol. Chem. 282*, 37854–37863.